Alma Mater Studiorum Università di Bologna
Archivio istituzionale della ricerca

A degraded adhesion model for creep force calculation based on the CONTACT algorithm

A degraded adhesion model for creep force calculation based on the CONTACT algorithm

Zhiyong Shi[1], Martina Meacci[1], Margherita Porcelli[2], Enrico Meli[1] and Andrea Rindi[1]

Abstract

Degraded adhesion is observed extensively during the braking or traction process. An accurate degraded adhesion law, on the other hand, is difficult to acquire since it is characterized by a complicated non-linear behaviour involving various surface phenomena. This work provides a new local degraded adhesion model, its implementation in a wheel-rail contact model, and its application in a multibody railway vehicle model. The present degraded adhesion model takes into account large sliding and adhesion recovery phenomena, which are strictly related to the power dissipated at the contact interface. Implementation of the current local degraded adhesion model enhances Kalker's CONTACT algorithm. The application into multibody dynamics simulation demonstrates the high accuracy of computations. The model is validated by comparing it to experimental findings obtained from on-field tests. Simulated results regarding the tangential pressures, the slip velocity, and the dissipated power under degraded adhesion and partial adherence conditions are reported.

Keywords
Adhesion recovery, Creep forces, Degraded adhesion, Multibody modelling, Wheel-rail contact model

Introduction

The evaluation of creep forces at the wheel-rail contact interface is fundamental in railway system dynamics. The foundation work by Kalker[1–3] on the modern wheel-rail rolling contact field is one of the most notable modelling strategies to face rolling contact problems. Kalker's theories, including the Linear theory, the Exact theory, and the Simplified theory, have been applied widely and improved gradually to face new challenges. For example, the algorithms FASTSIM and CONTACT were proposed to investigate railway vehicle simulations. A survey of different implementations, comparisons, and innovative improvements based on Kalker's theories can be found in[4–8].

Degraded adhesion extensively exists in the wheel-rail contact interface, especially during the braking or traction process of an operating train[9,10]. Degraded adhesion can result from complex conditions in reality. Experimental investigations have revealed that the adhesion coefficient is related to several macroscopic factors such as the train speed, the axle load, and the temperature[11–13], as well as various microscopic factors including the surface roughness, the surface contaminated layer parameters, the third body particle and others[14–16].

In degraded adhesion conditions, the relationship between creepage and creep force shows high non-linearity. Assumptions based on one small-creepage limitation, applied for the dry friction condition, limited simulation accuracy for further investigations. Under the premise of balancing the calculation efforts, revising this assumption can significantly improve the accuracy of a wheel-rail contact model. Therefore, it has attracted the attention of many researchers[17–21]. For example, Polach[22] proposed an algorithm for modelling creep forces at large creepage under low adhesion conditions, improving the simulation accuracy and the computational effort remarkably. The Polach contact theory has been further employed to assess the vehicle performance[23]. A degraded adhesion model has been presented in recent years, taking into consideration the power dissipation at the contact interface due to the large

[1]University of Florence, Italy
[2]University of Bologna, Italy

Corresponding author:
via Santa Marta, 3, Florence, Italy.
Email: enrico.meli@unifi.it

sliding and the resulting cleaning effect. Previous research focused on global degraded adhesion models [18,24,25] and a local degraded adhesion model [26–28] which directly connects local sliding/creepages inside the contact area and local pressures using the modified Kalker's FASTSIM algorithm. The current work continues the path by presenting a local degraded adhesion model based on the CONTACT algorithm, which promises higher accuracy.

This model can be used in a general planar-contact situation and has been validated through experiments, with a satisfying compromise between accuracy and efficiency. The current paper is organized as follows: the formulation, the algorithm, and the modelling methods are firstly introduced in the next section. Then, the validation of the model is detailed. The simulation results and discussion based on the proposed model are shown, and finally, the conclusion is drawn.

Modelling

In this chapter, the physical model of the wheel-rail contact system will be firstly defined. The planar mesh and the shape functions usually exploited to discretize the physical rolling contact problem will be briefly introduced next. Then, the local degraded adhesion model will be detailed. The CONTACT algorithm [29] will next be introduced and extended. Finally, the multibody system model will be presented. The following equations 1 to 13 have been published in [29]. As the critical modelling parts, they are referenced in this article for a complete introduction to the current model. For more details about Kalker's exact contact model, refer to [29–31].

Physical model of contact bodies

Usually, in the multibody simulation of mechanical systems, the contact bodies are considered globally rigid and locally deformable according to the linear elasticity theory for homogenous isotropic bodies (the so-called large displacement - small deformation approach) [32].

The inputs and definitions For the contact model, the main inputs are the kinematics of the bodies (position and velocities of the gravity centres $\mathbf{G}_1$, $\mathbf{G}_2$, $\mathbf{V}_{G1}$, $\mathbf{V}_{G2}$, rotation matrices $\mathbf{R}_1$, $\mathbf{R}_2$ and angular velocities ω_1, ω_2), the bodies geometries (volumes V_1, V_2 and contact surfaces S_1, S_1) and the bodies physical characteristics. All these inputs are provided by the multibody vehicle model of the system, (see Figure 1(a)). Starting from

the inputs, the following geometric and physical quantities can be easily calculated: the potential contact area A_c (i.e. the area on the contact plane where the rigid undeformed surfaces S_1, S_2 penetrate each other), the rigid penetration h (how much the rigid undeformed surfaces S_1, S_2 penetrate each other) and rigid local sliding $\mathbf{c} = \dot{\mathbf{x}}^1 - \dot{\mathbf{x}}^2$.

Assuming the contact is planar, a common tangent plane containing the contact area can be defined (Figure 1(b)); in such plane, the main contact reference frame is placed (origin in the point C, z-axis orthogonal to the contact plane and x-axis, y-axis on the plane). In the following, $\mathbf{x}^1$, $\mathbf{x}^2$ will be the underformed positions of the corresponding points on the undeformed contact surfaces S_1, S_2 (with outgoing unit normal vectors $\mathbf{n}^1$, $\mathbf{n}^2$) whereas $\mathbf{x}^1 + \mathbf{u}^1$, $\mathbf{x}^2 + \mathbf{u}^2$ will be the related deformed positions (see Figure 1(c)). As a consequence, the velocities of the undeformed particles are defined as $\dot{\mathbf{x}}^1$, $\dot{\mathbf{x}}^2$ (i.e. the velocities of the points $\mathbf{x}^1$, $\mathbf{x}^2$ rigidly connected to the contact bodies) and the velocities of the deformed particles as $\dot{\mathbf{v}}^1 = \dot{\mathbf{x}}^1 + \dot{\mathbf{u}}^1$, $\dot{\mathbf{v}}^1 = \dot{\mathbf{x}}^1 + \dot{\mathbf{u}}^1$.

The contact constraint Basing on the definitions of the rigid penetration h, the elastic penetration e, the contact pressures $\mathbf{p}_T$, and the mean contact position $\mathbf{x}$, we have the following inequalities (see Figure 2(a)):

$$e(\mathbf{x}) \geq 0 : \quad \text{either a gap or contact}$$
$$p_N(\mathbf{x}) \geq 0 : \quad \text{either no or a compressive normal traction} \tag{1}$$

where p_N and $\mathbf{p}_T$ are the normal and tangential components of the contact pressures $\mathbf{p}_T$. This formulation leads to the subdivision of the potential contact areas A_c into two disjointed regions: the real contact area C where $e = 0$ and the normal pressures p_N may be positive and the non-contact area E where $e > 0$ and $p_N = 0$. The contact constraint can be formulated as:

$$e \cdot p_N = 0 \tag{2}$$

The friction model The classic Coulomb-like friction law can be stated as:

$$|p_\tau| \leq g\left(p_z, |s_\tau|, \dots\right) \tag{3}$$

$$\text{if} \quad |s_\tau| \neq 0 \quad \Rightarrow \quad p_\tau = -g s_\tau / |s_\tau| \tag{4}$$
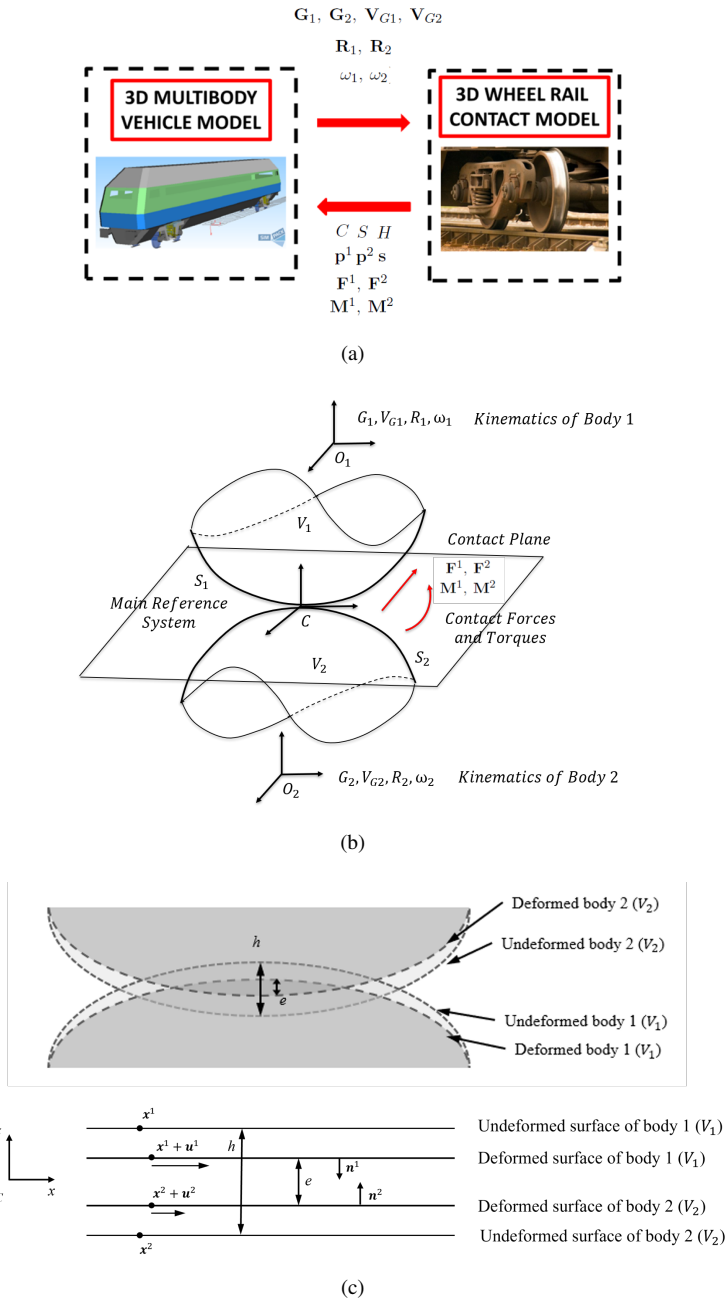
Figure 1. Modelling of wheel-rail contact (a) general architecture, (b) contact bodies, and (c) the distance

where p_τ, s_τ are the generic components of **p** and **s** respectively (here $\tau = x, y$), $p_z = p_N$ (according to the choice of the contact reference system in Figure 1(b)) and g is a general friction limit function assuming usually the following shape:

$$g\left(p_z, |s_\tau|, \ldots\right) = \mu\left(|s_\tau|, \ldots\right)p_z \tag{5}$$

in which μ is the friction characteristics. The Coulomb-like frictions model leads again to a subdivision of the contact areas C into two disjointed regions: the sliding contact area S where $|s_\tau| \neq 0$ and $p_\tau = -gs_\tau / |s_\tau|$ and the adhesion area H where $|s_\tau| = 0$ and $|p_\tau| \leq g\left(p_z, |s_\tau|, \ldots\right)$ (see Figure 2(a)).

The elasticity equations According to Navier's elasticity equations for homogeneous, isotropic, linear elastic bodies[32]:

$$\sigma_{ij} = \sigma_{ji} \quad \text{and} \quad \sigma_{ij,j} = 0 \tag{6}$$

where the classic Hooke's law connects the stress tensor σ_{ij} to the strain tensor e_{ij} in the case of an isotropic material:

$$e_{ij} = \frac{1+\nu}{E}\sigma_{ij} - \frac{\nu}{E}\delta_{ij}\sigma_{kk}, \quad \sigma_{ij} = \frac{Ee_{ij}}{1+\nu} + \frac{E\delta_{ij}e_{kk}}{(1+\nu)(1-2\nu)} \tag{7}$$

in which $i, j = 1, 2, 3$, E is the Young's elasticity modulus and ν is the Poisson's coefficient. Such model has been exploited in this work to describe both body 1 and body 2. Under the working hypotheses of non-conformal contact, planar contact and half-space contact, the Navier's elasticity equations can be analytically solved[29]. More precisely, it is possible to explicitly write the unknown elastic deformations **u** as a function of the pressures on the contact area **p** through suitable shape functions $A_{ik}(\mathbf{x}, \mathbf{y})$:

$$u_i(\mathbf{x}) = \int_{\partial V} A_{ik}(\mathbf{x}, \mathbf{y})p_k(\mathbf{y})dS(\mathbf{y}) \tag{8}$$

where $A_{ik}(\mathbf{x}, \mathbf{y})$ can be determined analytically according to the Bossinesq-Cerruti solution. The derivations can be found in[29].

The contact problem formulation Eq. (9) summarizes the contact model described above:

$$
\begin{aligned}
&\text{in } C: e = 0, \quad p_N \geq 0 \\
&\text{in } E: \mathbf{p} = 0, \quad e > 0 \\
&C \cup E = A_c, \quad C \cap E = \varnothing \\
&\text{in } H: \qquad\quad |s_I| = 0, \quad |p_I| \leq g \\
&\text{in } S: \qquad\quad\; |s_I| \neq 0, \quad \mathbf{p}_I = -g s_I / |\mathbf{s}_I| \\
&S \cup H = C, \quad S \cap H = \emptyset
\end{aligned}
\tag{9}
$$

where the first three rows represent the normal contact problem (calculation of the normal contact pressures p_N and of the shapes of A_C, C and E) whereas the second three rows the tangential contact problem (calculation of the tangential contact pressures and local slidings p_τ, s_τ with $p_\tau = x, y$ and of the shapes of S and A).

Planar mesh and shape functions

A planar quadrilateral mesh is used to discretize A_c, as shown in Figure 2(b). Define $\mathbf{x}_I = (x_I, y_I, 0)$, where I identifies the specific element. The discrete values of the elastic deformation $\mathbf{u}$ on the mesh nodes at the present time step t and at the past time step t' will be:

$$
\begin{aligned}
\mathbf{u}_I &= (u_{Ii}) = (u_I, v_I, w_I) \quad \text{at} \quad (\mathbf{x}_I, t) \\
\mathbf{u}'_I &= (u'_{Ii}) = (u'_I, v'_I, w'_I) \quad \text{at} \quad (\mathbf{x}_I + \mathbf{v}(t - t'), t').
\end{aligned}
\tag{10}
$$

For the contact pressures $\mathbf{p}$:

$$
\begin{aligned}
\mathbf{p}_J &= (p_{Jj}) = (p_{xJ}, p_{yJ}, p_{zJ}) \quad \text{at} \quad (\mathbf{x}_J, t) \\
\mathbf{p}'_J &= (p'_{Jj}) = (p'_{xJ}, p'_{yJ}, p'_{zJ}) \quad \text{at} \quad (\mathbf{x}_J + \mathbf{v}(t - t'), t').
\end{aligned}
\tag{11}
$$

The discretized displacements $\mathbf{u}_I$:

$$
\begin{aligned}
u_{Ii} &= \sum_{J=1}^{N} \sum_{j=1}^{3} A_{IiJj} p_{Jj} \\
u'_{Ii} &= \sum_{J=1}^{N} \sum_{j=1}^{3} C_{IiJj} p'_{Jj}
\end{aligned}
\tag{12}
$$

where
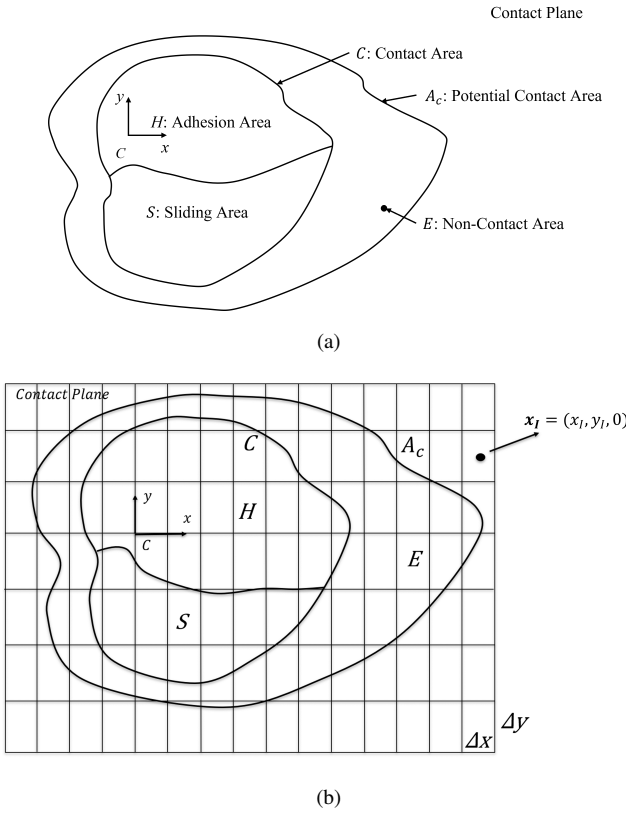
Figure 2. Contact area: (a) subdivision and (b) discretization

$$
\begin{aligned}
A_{IiJj} &= B_{IiJj}\left(\mathbf{x}_I\right) \\
C_{IiJj} &= B_{IiJj}\left(\mathbf{x}_I + \mathbf{v}\left(t - t'\right)\right)
\end{aligned}
\tag{13}
$$

and B_{IiJj} are the discrete shape functions of the problem that describe the effect of a contact pressure $\mathbf{p}_J$ applied to the element J on the displacement $\mathbf{u}_I$ of the node I. The shape function B_{IiJj} depends usually on the problem geometry and the characteristics of the materials (Young's modulus E, shear modulus G and Poisson's coefficient ν). See[29] for derivations.

Local degraded adhesion model

In general, sliding occurs under degraded adhesion conditions and it is responsible for the material removal at the contact interface in a contaminated environment. This cleaning effect leads to an increase in the adhesion coefficient. This is mostly due to the dissipated power during the sliding process. When the dissipated power, W_{sp}, is minimal, the cleaning effect is non-existent, the contamination level h remains constant, and the friction coefficient μ remains constant. As W_{sp} accumulates, the cleaning effect increases, the contamination level h thins, and the friction coefficient rises. Eventually, the sustained recovery process ends with the removal of all contaminants, and the friction coefficient μ attains its maximum value μ_r. If W_{sp} diminishes, the opposite process happens.

Figure 3 approximately illustrates μ as a function of slip velocity, which includes (a) a general situation and (b) in the presence of dissipated power W_{sp}, where μ_a and μ_c are the static and the kinematic friction coefficients; μ_d and μ_r are the friction coefficients in degraded adhesion and adhesion recovery conditions; μ_{cd} and μ_{cr} are the kinematic values corresponding to the static μ_d and μ_r values.
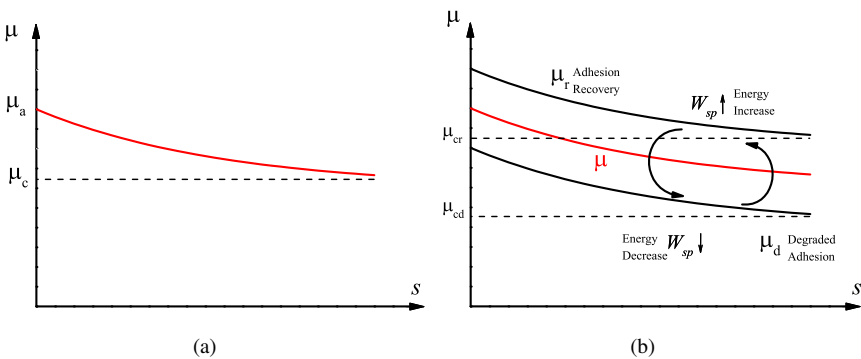

Figure 3. The friction coefficient μ as function of slip velocity s: (a) standard and (b) in presence of dissipated power W_{sp} at the contact interface [28]

We propose the following equation for μ to recreate the quantitative trend in Figure 3(b):

$$\mu = [1 - \lambda(W_{sp})]\mu_d + \lambda(W_{sp})\mu_r \quad (14)$$

where $\lambda(W_{sp})$ is a transition function of the dissipated power W_{sp}, between degraded adhesion and adhesion recovery. $\lambda(W_{sp})$ must meet the conditions of being both positive and monotonous rising, and satisfy the following boundary conditions:

$$\begin{cases} \lambda(0) & = 0 \\ \lambda(+\infty) & = 1 \end{cases} \tag{15}$$

For $\lambda(W_{sp})$, we use the following expression:

$$\lambda(W_{sp}) = 1 - e^{-\tau|W_{sp}|} \tag{16}$$

where τ is a parameter to be adjusted based on experimental data. The value of τ is found usually between 4×10^{-9} and 3×10^{-8}, with the unit m^2/W, given reference in[27]).

Combining Eqs. (16) and (14), for a point (x_I, y_I) in the discretized area, the following equations for determining its friction coefficient μ through μ_d and μ_r can be written as

$$\begin{cases} \mu_d(x_I, y_I) = (\frac{\mu_{cd}}{A_d} - \mu_{cd})e^{-s(x_I,y_I)\gamma_d} + \mu_{cd} \\ \mu_r(x_I, y_I) = (\frac{\mu_{cr}}{A_r} - \mu_{cr})e^{-s(x_I,y_I)\gamma_r} + \mu_{cr} \end{cases} \tag{17}$$

$$\begin{cases} \mu(x_I, y_I) = (1 - \lambda)\mu_d(x_I, y_I) + \lambda\mu_r(x_I, y_I) \\ \lambda = 1 - e^{-\tau|W_{sp}|} \end{cases} \tag{18}$$

where $s = \|\mathbf{s}\|$, A_d and A_r are the ratios between the kinetic and the static friction coefficients, and γ_d and γ_r are the friction decrease rates. W_{sp} is calculated as follows:

$$W_{sp}(x_I, y_I) = \mathbf{p_T}(x_I, y_I) \cdot \mathbf{s}(x_I, y_I) \tag{19}$$

According to Coulomb's law, tangential contact pressures $\mathbf{p_T}$ and local sliding $\mathbf{s}$, are represented as follows:

if (x_I, y_I) in H

$$\begin{cases} |\mathbf{s}(x_I, y_I)| = & 0 \\ |\mathbf{p_T}(x_I, y_I)| \leq & \mu(x_I, y_I) \cdot p_N(x_I, y_I) \end{cases} \tag{20}$$

if (x_I, y_I) in S

$$\begin{cases} |\mathbf{s}(x_I, y_I)| \neq & 0 \\ \mathbf{p_T}(x_I, y_I) = & -\mu(x_I, y_I) \cdot p_N(x_I, y_I)\frac{\mathbf{s}(x_I,y_I)}{|\mathbf{s}(x_I,y_I)|} \end{cases} \tag{21}$$

Modified CONTACT algorithm

The inputs of the CONTACT algorithm[29] are the potential contact area A_c, the rigid penetration h and the rigid local sliding $\mathbf{c}$. With the inputs, the NORM algorithm determines real contact area C, non-contact area E, normal contact pressures p_N. With the results from NORM algorithm, the TANG algorithm then calculates sliding area S, adhesion area H, tangential contact pressures $\mathbf{p_T}$ and local sliding $\mathbf{s}$. The results of the TANG algorithm are then passed back to NORM algorithm to correct and improve the evaluation of the normal pressures p_N. At each time step, the contact pressures p_N, $\mathbf{p_T}$ are stored to be used at the following time step to estimate the time derivatives of the elastic deformation $\mathbf{u}$ involved in the calculation of the local sliding $\mathbf{s}$.

This Chapter presents the modified CONTACT algorithm. The NORM algorithm is retained while the TANG algorithm is improved. In the modified TANG algorithm, the local adhesion model is inserted.

The NORM algorithm According to the considered discretization procedure, at each node $\mathbf{x_I}$, the elastic penetration e is

$$e_I = h_I + w_I \tag{22}$$

whereas the normal part of the contact constraint becomes

$$p_{Iz} \geq 0, \quad w_I \geq 0, \quad p_{Iz}w_I = 0. \tag{23}$$

The algorithm to calculate the normal contact pressure p_N and, at the same time, to build the real contact area C and the non-contact area E inside the potential contact area A_c can be summarized in the following steps:

1. set $h_I^* = h_I + \sum_{J,\tau} A_{I3J\tau}p_{J\tau}, \forall x_I \in A_c$;
2. set $p_{Jz} = 0 \quad \forall J$; clear all normal tractions;
3. initially, the non-contact area $E = Q$, and the real contact area $C = \emptyset$; E and C are modified until they correspond to the solution;
4. during the procedure, $e_I = 0 \quad \forall x_I \in C, p_{Jz} = 0 \quad \forall x_J \in E$; these are N_C linear equations in the N_C unknowns p_{Jz} in the nodes of $\mathbf{C}$;

5. are all pressures $p_{Jz} \geq 0$ in C? If "no", go to Point 6; if "yes", go to Point 7;
6. if $p_{yz} < 0$, element J is placed in the non-contact zone E, and p_{Jz} is set equal to zero; go to Point 4;
7. are all elastic penetrations $e_I > 0$ in E? If "yes", END; if "no", place all elements with elastic penetrations < 0 in C; go to Point 4.

The TANG algorithm As in the previous case, the main physical quantities involved into the tangential contact problem can be calculated on the mesh nodes $\mathbf{x_I}$. The tangential components of the elastic displacements both at current and at the past time steps (t and t') become

$$\begin{aligned} \boldsymbol{u_I} &= \sum_{\boldsymbol{J}} \sum_j A_{I1Jj} p_{Jj} \\ \boldsymbol{v_I} &= \sum_{\boldsymbol{J}} \sum_j A_{I2Jj} p_{Jj} \quad \text{at } (\mathbf{x}_I, t) \end{aligned} \tag{24}$$

$$\begin{aligned} u'_I &= \sum_J \sum_j C_{I1Jj} p'_{Jj} \\ v'_I &= \sum_J \sum_j C_{I2Jj} p'_J \quad \text{at } (\mathbf{x}_I + \mathbf{v}(t - t'), t'). \end{aligned} \tag{25}$$

On the other hand, the local sliding **s** can be discretized by properly approximating the time derivative of the elastic deformation $\dot{\mathbf{u}}$:

$$\mathbf{s}_I = \mathbf{c}_I + \frac{(\mathbf{u}_I - \mathbf{u}'_I)}{t - t'}. \tag{26}$$

The general friction limit function takes the following form:

$$g_I = \mu_I p_{Iz} \tag{27}$$

whereas the μ_I is expressed in Eq. (18), and the Coulomb-like friction model can be further expressed as follows (i.e. the tangential part of the contact constraint):

$$\begin{aligned} &|(p_{I1}, p_{I2})| \leq g_I \\ &\text{if the inequality holds: } (s_{I1}, s_{I2}) = 0 \\ &\text{if the equality holds: } (s_{I1}, s_{I2}) = -|(s_{I1}, s_{I2})| (p_{I1}, p_{I2}) / g_I \end{aligned} \tag{28}$$

The algorithm to calculate the tangential contact pressures $\mathbf{p_T}$ and local sliding $\mathbf{s}$ and, at the same time, to build the adhesion area H and the sliding area S inside the real contact area C can be summarized in the following steps:

1. set $(p_{I1}, p_{I2}) = (0, 0)$; clear the tangential contact pressures;
2. initially, $S = \emptyset$, $H = C$; during the procedure, $H \cup S = C$ until they correspond to the solution;
3. solve:
   $(s_{I1}, s_{I2}) = 0$, these are $2N_H$ linear equations on the nodes of the adhesion area H in the $2N_H$ unknowns;
   $(s_{I1}, s_{I2}) = -|(s_{I1}, s_{I2})|(p_{I1}, p_{I2})/\mu_I p_{Iz}$; these are $2N_S$ non-linear equations on the nodes of the sliding area S in the $2N_S$ unknowns (p_{I1}, p_{I2});
   note that μ_I is a function of (s_{I1}, s_{I2}) and (p_{I1}, p_{I2}), and can be calculated according to Eqs. 17 - 21, by coupling such equations to the original tangential pressure equations $(s_{I1}, s_{I2}) = -|(s_{I1}, s_{I2})|(p_{I1}, p_{I2})/\mu_I p_{Iz}$;
4. if $|p_{I1}, p_{I2}| > g_I$, for every node in H, place element I in the sliding area S, if this has happened at least once, go back to Point 5;
5. if the slip (s_{I1}, s_{I2}) is in the same sense as the tangential traction (p_{I1}, p_{I2}) rather than opposite as it should be in the sliding area, then place element I in the adhesion area H;
   if this has happened at least once, go back to Point 3, else END.

The local degraded adhesion model based on modified CONTACT algorithm is implemented in Fortran and interacted with SIMPACK by generating new routines. Figure 4 shows an architecture of the modified CONTACT model. We use the tolerance on the absolute value of main quantities (e.g. the shape of the contact area) as the criterion. Once the convergence is reached, the final values of normal and tangential pressures p_N, $\mathbf{p_T}$ are available. Finally, the contact forces and torques exchanged by the contact bodies are determined by simple numerical integration and sent back to the time integrator to carry on the simulation of the multibody system.

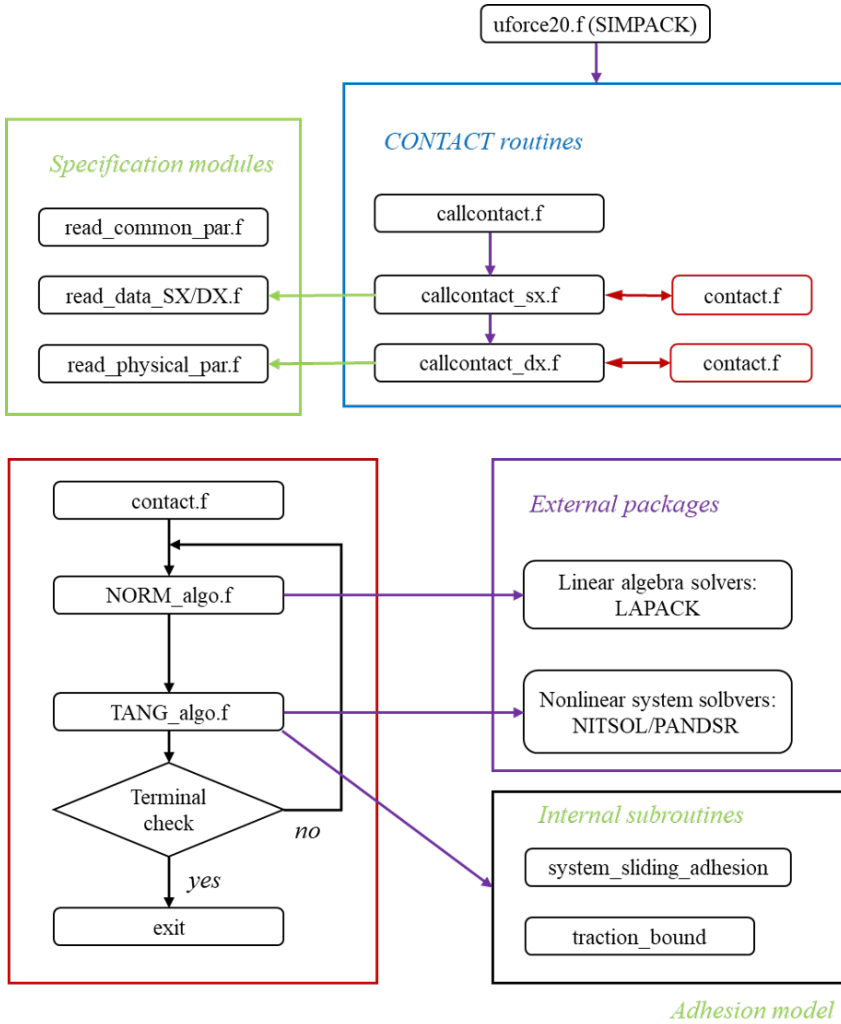**Figure 4.** Modified CONTACT model

Multibody system model

The multibody vehicle model is developed according to the UIC-Z1 vehicle[33]. The 50-degree-of-freedoms multibody vehicle model is generated, which includes 1 carbody, 2 bogie frames, 4 wheelsets and 8 axle boxes. The Wheel Slide Protection (WSP) system of the railway vehicle UIC-Z1 has been modelled to better investigate the vehicle

behaviour during the braking under degraded adhesion conditions. The wheel thread and rail profile are ORE S 1002 and UIC 60.

Table 1 lists the main parameters of the railway vehicle for MBS simulation.

Table 1. Main parameters of the railway vehicle

Description		Unit	Value
Carbody mass		kg	29000
Carbody rotary inertias	Roll	$kg \cdot m^2$	76400
	Pitch	$kg \cdot m^2$	1494400
	Yaw	$kg \cdot m^2$	1467160
Bogie frame mass		kg	3000
Bogie frame rotary inertias	Roll	$kg \cdot m^2$	2400
	Pitch	$kg \cdot m^2$	1900
	Yaw	$kg \cdot m^2$	4000
Wheelset mass		kg	1300
Wheelset rotary inertias	Roll	$kg \cdot m^2$	800
	Pitch	$kg \cdot m^2$	160
	Yaw	$kg \cdot m^2$	800
Axlebox mass		kg	200
Wheelset rotary inertias	Roll	$kg \cdot m^2$	3
	Pitch	$kg \cdot m^2$	12
	Yaw	$kg \cdot m^2$	12
Wheelset spacing		m	2.56
Bogie spacing		m	19
Wheel diameter		m	0.89

Validation

Even though the validation of an adhesion model regarding contact pressures would be direct, the difficulty makes the measurements almost impossible. As an alternative, we compare experimental and simulated results regarding velocities, forces, and global sliding so as a good compromise to get a preliminary validation. The data for the validation of the extended CONTACT model are from the experimental campaign performed by Trenitalia in Velim, Czech Republic, with the vehicle UIC-Z1, following the UIC 541-05 regulations[34]. The vehicle

under consideration is equipped with a fully-working WSP system that modulates the braking force, in order to control the slip value. The experimental tests have been carried out on a straight railway track without turnouts, and the profiles did not present relevant amount of wear after the braking.

In Table 2, the main contact characteristics are reported. The Young modulus, shear modulus, and the Poisson coefficient for the wheel material and the rail material are considered the same. The contact damping constant is a parameter that allows to calculate the part of the normal force proportional to the penetration velocity, according to the Hertz theory[35]. The kinetic friction coefficient under degraded adhesion conditions μ_{cd} depends on the test from the track (see[18,36]). The kinetic friction coefficient under full adhesion recovery μ_{cr} depends on the wheel and rail material and represents the kinetic friction coefficient under dry conditions.

Table 2. Main contact characteristics

Parameters	Unit	Value
Young modulus	Pa	2.1×10^{11}
Shear modulus	Pa	8×10^{10}
Poisson coefficient	-	0.3
Contact damping constant	$N \cdot s/m$	1×10^5
Kinetic friction coefficient μ_{cd}	-	0.06
Kinetic friction coefficient μ_{cr}	-	0.28
Friction ratio A_d	-	0.4
Friction ratio A_r	-	0.4
Friction decrease rate γ_d	s/m	0.2
Friction decrease rate γ_r	s/m	0.6

The experimental data used to calculate the wheel–rail adhesion coefficient are derived from a set of 27 braking tests, 11 of which were performed with a single vehicle. During the experiments, the following physical quantities were measured:

- the longitudinal vehicle velocity v_v^{sp};
- the rotation velocities of all the wheels ω_{wj}^{sp};
- the vertical loads N_{wj}^{sp} on the wheels;
- the traction or braking torques C_{wj}^{sp} applied to the wheels.

Figure $5(a)$ exhibits the results on comparing the time histories of the velocities v_v^{sm}, v_v^{sp} (simulated and experimental of the vehicle, respectively), and $r\omega_{w1}^{sm}$, $r\omega_{w1}^{sp}$ (simulated and experimental of the first wheelset, respectively). Degraded adhesion phenomenon is revealed by the difference between the vehicle velocity and the wheel velocity. Two groups of velocities v_v^{sm} and v_v^{sp}, $r\omega_{w1}^{sm}$ and $r\omega_{w1}^{sp}$ are well matched. During the braking, there is a significant difference between the slopes before and after the instant t=25 s. The change of slope in the second part of the simulation depicts the braking maneuver's adhesion recovery. Figure $5(a)$ shows the difference between the vehicle velocity and the wheel velocity during the braking process. The difference reaches maximum at near $t = 17s$, exceeding $5m/s$. This is seen due to the fact that the severely degraded adhesion phenomenon occurred at the current instant. Figure $5(d)$ shows a significant difference between the measured and the simulated values in the time histories. This is because the sliding velocity cannot be locally compared to each other. Because a realistic railway system includes non-linear elements (like WSP), bringing out high complexity, which restricts the possibility of measuring corresponding quantities.

In Figures $5(b)$, $5(c)$ and $5(d)$, the trends of the experimental and simulated adhesion coefficient, the longitudinal contact forces, and the sliding are shown. The experimental and simulated adhesion coefficient is calculated by $f_j^{sp} = T_{cj}^{sp}/N_{cj}^{sp}$, $f_j^{sm} = T_{cj}^{sm}/N_{cj}^{sm}$, where T_{cj}^{sp} and T_{cj}^{sm} are approximately estimated as $I_j^{sm/sp}\vec{\omega}_{wj}^{sm/sp}=C_{wj}^{sm/sp} - T_{wj}^{sm/sp} \cdot r$. In Figure $5(d)$, the slip velocity of the simulated and the experimental ones are calculated by $s_j^{sm} = v_v^{sm} - r\omega_{wj}^{sm}$ and $s_j^{sp} = v_v^{sp} - r\omega_{wj}^{sp}$. We can see that Figures $5(b)$ and $5(c)$ both emphasise the adhesion recovery that occurs during the second part of the braking. Two groups of adhesion coefficients and longitudinal contact forces are also well matched.

For the sliding in Figure $5(d)$, in the first part of the simulation, there is an obvious difference between the simulated and experimental values. It can be due to the imperfect coincident time of application of the braking torque and particularly to the difficulty to predicting the moment of the first loss of adherence of the wheels.
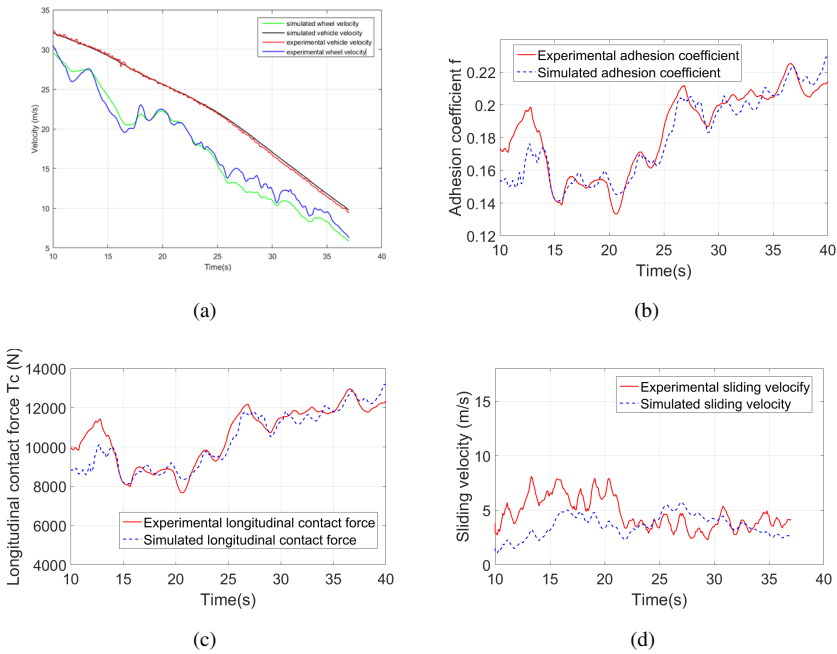
Figure 5. Comparison between experimental and simulated results of (a) velocity, (b) adhesion coefficient, (c) longitudinal contact force, and (d) sliding velocity

Numerical results and discussion

This section presents simulated results on several contact variables. Two simulation instants are considered: one at 12s (when lower sliding occurs and partial adherence is present) and one at 27s (when higher sliding occurs and degraded adhesion conditions exist). Results are corresponding to the left wheel of the first wheelset. The longitudinal and lateral components of the tangential contact pressures $\vec{p_t}$ under a partial adherence condition (PAC) and a pure sliding condition (PSC) are presented in Figure 6. Note that, under the pure sliding condition, the lateral tangential stress is at a low level, compared to the longitudinal tangential stress. As the value of tangential stress is affected by the creepages (longitudinal, lateral and spin creepages), the longitudinal creepage is much larger than the lateral and spin creepages. When the spin creepage is in a certain range, both positive and negative components
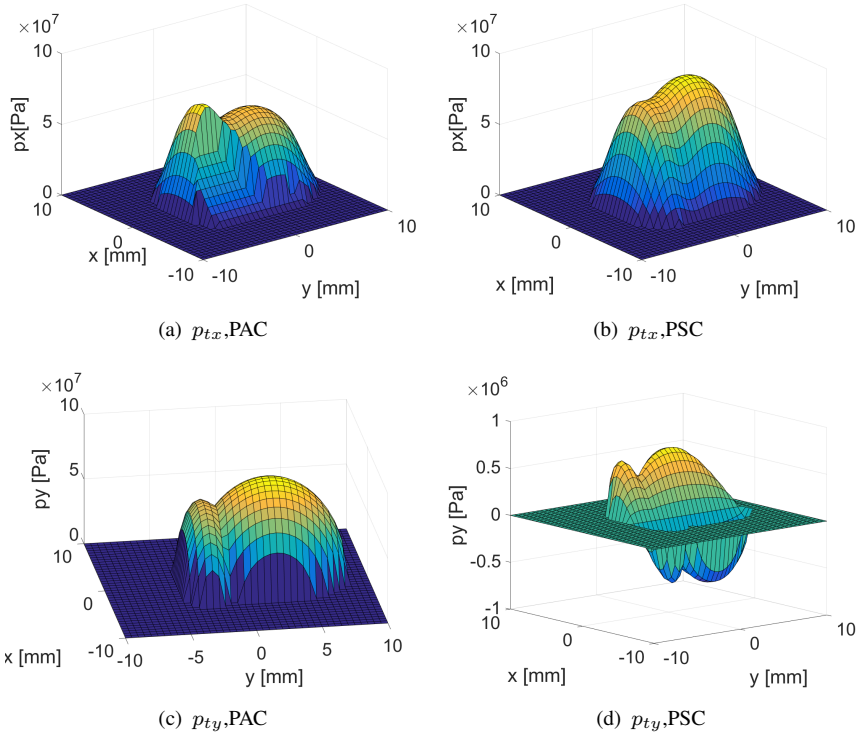
(a) p_{tx},PAC

(b) p_{tx},PSC

(c) p_{ty},PAC

(d) p_{ty},PSC

Figure 6. Comparison of the tangential pressures for partial adherence condition and pure sliding condition

will be generated for the lateral tangential stress. Therefore, Figure 6(d) shows both positive and negative values of the lateral tangential stress.

Similarly, Figure 7 depicts the longitudinal and lateral components of the local sliding $\vec{s}$ at 12s and 27s. Figure 8 plots the dissipated power W_{sp} inside the contact patch under two different contact conditions.

It can be seen that as the W_{sp} is directly connected with the sliding, the value of W_{sp} reaches the maximum in a pure sliding condition, while it is zero in the presence of adherence. To combine Figures 6 to 8, regarding the contact patch, we do not notice a visible change in the two different instants chosen because one of the main parameters that influences the shape is the lateral displacement, and the case of straight line simulations is of current concern. When partial adherence is present, both adhesion area and slip area are present in Figures 6(a), 6(c), 7(a)
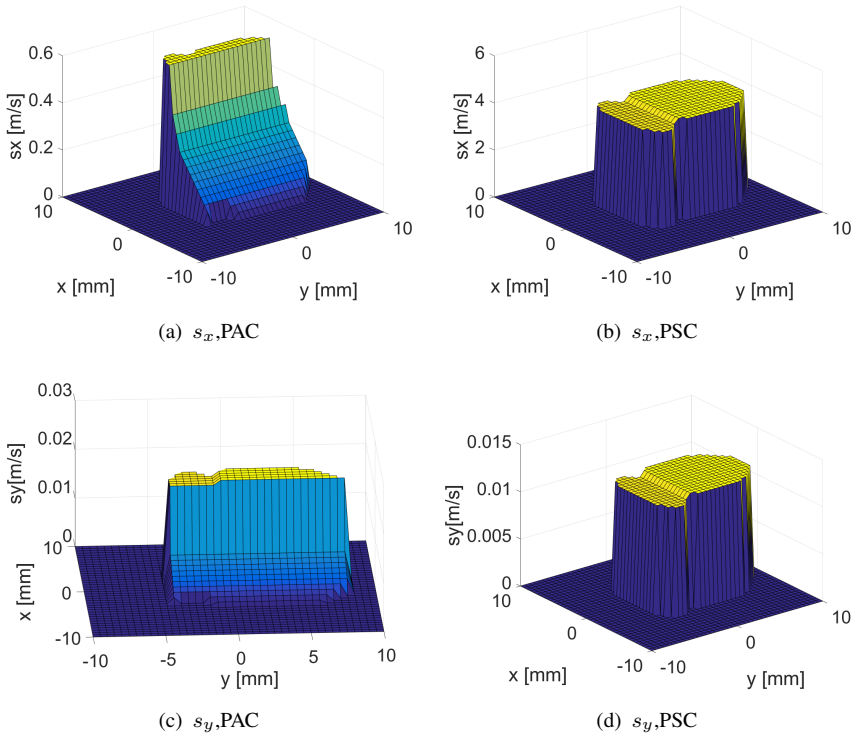
(a) s_x,PAC

(b) s_x,PSC

(c) s_y,PAC

(d) s_y,PSC

Figure 7. Comparison of the slip velocity for partial adherence condition and pure sliding condition
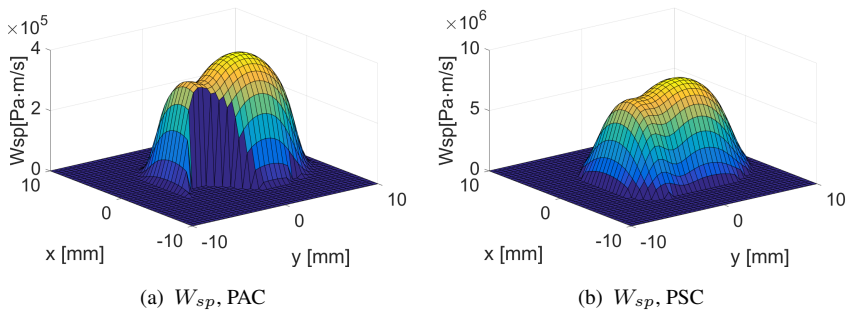

(a) W_{sp}, PAC

(b) W_{sp}, PSC

Figure 8. Comparison of the dissipated power for partial adherence condition and pure sliding condition

and 7(c). The tangential pressures p_{tx} and sliding s_x in Figures 6(b), 6(d), 7(b) and 7(d) clearly highlights the presence of the only slip area inside the contact patch. Dissipated power W_{sp} is consistent with p_t and s: the power dissipation is concentrated in the slip area and higher sliding leads to higher dissipated power.

Conclusions and future work

In this paper, the authors established a degraded adhesion model for creep force calculation. The new model has extended the CONTACT algorithm, by considering the adhesion law in a more general situation. The tangential contact pressure is determined locally while accounting for large sliding and adhesion recovery phenomena. The integration of the modified CONTACT algorithm developed in a Fortran environment with the general vehicle multibody models as well as the local adhesion model is thoroughly presented. Experimental tests have been performed on a straight railway track with a vehicle equipped on every wheelset with a WSP system. The comparison between experimental and simulated results on adhesion coefficient, longitudinal contact force and sliding validate the model. Finally, tangential pressures, slip velocity, and dissipated power under degraded adhesion and partial adherence conditions are reported.

Future developments may include the investigation into conformal contact behaviour, as well as its experimental validation, which will require a consideration of non-planar conditions. Furthermore, the authors would comprehensively compare the differences, pros, and cons of the current model with the global degraded adhesion model, and the local degraded adhesion model based on FASTSIM that has been proposed in previous publications.

Acknowledgements

References

1. Kalker JJ. *On the rolling contact of two elastic bodies in the presence of dry friction.* PhD Thesis, TU Delft, Delft University of Technology, 1967.
2. Kalker J. A fast algorithm for the simplified theory of rolling contact. *Vehicle system dynamics* 1982; 11(1): 1–13.

3. Kalker J. Survey of wheel—rail rolling contact theory. *Vehicle system dynamics* 1979; 8(4): 317–358.

4. Meymand SZ, Keylin A and Ahmadian M. A survey of wheel–rail contact models for rail vehicles. *Vehicle System Dynamics* 2016; 54(3): 386–428.

5. Spiryagin M, Polach O and Cole C. Creep force modelling for rail traction vehicles based on the fastsim algorithm. *Vehicle System Dynamics* 2013; 51(11): 1765–1783.

6. Vollebregt E and Wilders P. Fastsim2: a second-order accurate frictional rolling contact algorithm. *Computational Mechanics* 2011; 47(1): 105–116.

7. Vollebregt E and Schuttelaars H. Quasi-static analysis of two-dimensional rolling contact with slip-velocity dependent friction. *Journal of Sound and Vibration* 2012; 331(9): 2141–2155.

8. Trummer G, Buckley-Johnstone L, Voltr P et al. Wheel-rail creep force model for predicting water induced low adhesion phenomena. *Tribology international* 2017; 109: 409–415.

9. Chen H, Ishida M and Nakahara T. Analysis of adhesion under wet conditions for three-dimensional contact considering surface roughness. *Wear* 2005; 258(7-8): 1209–1216.

10. Olofsson U. A multi-layer model of low adhesion between railway wheel and rail. *Proceedings of the Institution of Mechanical Engineers, Part F: Journal of Rail and Rapid Transit* 2007; 221(3): 385–389.

11. Chen H, Ban T, Ishida M et al. Adhesion between rail/wheel under water lubricated contact. *Wear* 2002; 253(1-2): 75–81.

12. Zhang W, Chen J, Wu X et al. Wheel/rail adhesion and analysis by using full scale roller rig. *Wear* 2002; 253(1-2): 82–88.

13. Spiryagin M, Wu Q, Duan K et al. Implementation of a wheel–rail temperature model for locomotive traction studies. *International Journal of Rail Transportation* 2017; 5(1): 1–15.

14. Chen H, Ban T, Ishida M et al. Experimental investigation of influential factors on adhesion between wheel and rail under wet conditions. *Wear* 2008; 265(9-10): 1504–1511.

15. Arias-Cuevas O, Li Z, Lewis R et al. Laboratory investigation of some sanding parameters to improve the adhesion in leaf-contaminated wheel—rail contacts. *Proceedings of the Institution of Mechanical Engineers, Part F: Journal of Rail and Rapid Transit* 2010; 224(3): 139–157.

16. Wang W, Liu T, Wang H et al. Influence of friction modifiers on improving adhesion and surface damage of wheel/rail under low adhesion conditions. *Tribology International* 2014; 75: 16–23.

17. Alturbeh H, Stow J, Tucker G et al. Modelling and simulation of the train brake system in low adhesion conditions. *Proceedings of the Institution of Mechanical Engineers, Part F: Journal of Rail and Rapid Transit* 2020; 234(3): 301–320.

18. Meli E and Ridolfi A. An innovative wheel–rail contact model for railway vehicles under degraded adhesion conditions. *Multibody System Dynamics* 2015; 33(3): 285–313.

19. Onat A, Voltr P and Lata M. A new friction condition identification approach for wheel–rail interface. *International Journal of Rail Transportation* 2017; 5(3): 127–144.

20. Spiryagin M, Cole C and Sun YQ. Adhesion estimation and its implementation for traction control of locomotives. *International Journal of Rail Transportation* 2014; 2(3): 187–204.

21. Vollebregt E, Six K and Polach O. Challenges and progress in the understanding and modelling of the wheel–rail creep forces. *Vehicle System Dynamics* 2021; 59(7): 1026–1068.

22. Polach O. Creep forces in simulations of traction vehicles running on adhesion limit. *Wear* 2005; 258(7-8): 992–1000.

23. Zirek A, Voltr P, Lata M et al. An adaptive sliding mode control to stabilize wheel slip and improve traction performance. *Proceedings of the Institution of Mechanical Engineers, Part F: Journal of Rail and Rapid Transit* 2018; 232(10): 2392–2405.

24. Allotta B, Meli E, Ridolfi A et al. Development of an innovative wheel–rail contact model for the analysis of degraded adhesion in railway systems. *Tribology International* 2014; 69: 128–140.

25. Pugi L, Ridolfi A, Malvezzi M et al. Three dimensional modelling of wheel–rail degraded adhesion conditions. In *22nd international symposium on dynamics of vehicles on roads and tracks*.

26. Meacci M, Shi Z, Butini E et al. A new local degraded adhesion model for railway applications including energy dissipation and adhesion recovery. In *11th International Conference on Contact Mechanics and Wear of Rail/wheel Systems*. pp. 711–719.

27. Meacci M, Shi Z, Butini E et al. A local degraded adhesion model for creep forces evaluation: An approximate approach to the tangential contact problem. *Wear* 2019; 440: 203084.

28. Meacci M, Shi Z, Butini E et al. A railway local degraded adhesion model including variable friction, energy dissipation and adhesion recovery. *Vehicle System Dynamics* 2020; : 1–22.

29. Kalker JJ. Rolling contact phenomena - linear elasticity. *CISM, International Centre for Mechanical Sciences*, Wien, New York: Springer, 2000. pp. 1–84.

30. Kalker JJ. *Three-dimensional elastic bodies in rolling contact*, volume 2. Springer Science & Business Media, 2013.

31. Cristina S. *Solving systems of nonlinear equations via spectral residual methods*, University of Florence, 2021.

32. Popov VL. *Contact mechanics and friction*. Springer, 2010.

33. TrenitaliaSpA. Uic-z1 coach. internal report of trenitalia. Technical report, Rome, Italy, 2000.

34. Council of European Union. Railway applications, braking, wheel slide protection. UNI EN 15595, 2009.

35. Auciello J, Meli E, Falomi S et al. Dynamic simulation of railway vehicles: wheel/rail contact analysis. *Vehicle system dynamics* 2009; 47(7): 867–899.

36. Meli E, Pugi L and Ridolfi A. An innovative degraded adhesion model for multibody applications in the railway field. *Multibody System Dynamics* 2014; 32(2): 133–157.